Chemosphere 346 (2024) 140585

Contents lists available at ScienceDirect

Chemosphere

journal homepage: www.elsevier.com/locate/chemosphere

Aqueous and solid phase photocatalytic degradation of perfluorooctane sulfonate by carbon- and Fe-modified bismuth oxychloride

Rayees Ahmad Rather [a], Tianyuan Xu [b], Rodney Nelson Leary III [a], Dongye Zhao [a,*]

[a] Department of Civil, Construction, And Environmental Engineering, San Diego State University, San Diego, CA, 92182, USA
[b] School of Resource and Geoscience, China University of Mining and Technology, Xuzhou, Jiangsu, 221116, China

HIGHLIGHTS

- A carbon-modified Fe-doped bismuth oxychloride photocatalyst Fe–BiOCl/CS was prepared.
- Fe–BiOCl/CS can rapidly and effectively adsorb PFOS from water.
- Fe–BiOCl/CS under UV (254 nm) can effectively degrade and defluorinate pre-sorbed PFOS.
- Fe–BiOCl/CS is reusable without chemical regeneration.
- Photoactivated electrons and superoxide radicals initiated desulfonation of PFOS.

GRAPHICAL ABSTRACT

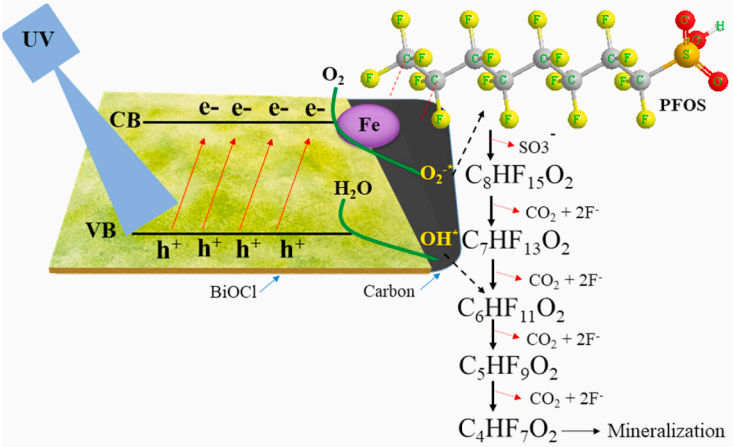

ARTICLE INFO

Handling editor: Y Yeomin Yoon

Keywords:
PFAS
Carbon-modified catalyst
Photocatalysis
Adsorption
Photodegradation

ABSTRACT

In this study, we prepared and tested a carbon-modified, Fe-loaded bismuth oxychloride (Fe–BiOCl/CS) photocatalyst for photocatalytic degradation of perfluorooctane sulfonate (PFOS). Structural analyses revealed a (110) facet-dominated sheet-type BiOCl crystal structure with uniformly distributed Fe and confirmed carbon modification of the photocatalyst. The presence of D-glucose facilitated the growth control of BiOCl particles and enhanced the adsorption of PFOS via added hydrophobic interaction. Adsorption kinetic and equilibrium tests showed rapid uptake rates of PFOS and high adsorption capacity with a Langmuir Q_{max} of 1.51 mg/g. When used for directly treating PFOS in solution, Fe–BiOCl/CS was able to mineralize or defluorinate 83% of PFOS (C_0 = 100 μgL^{-1}) under UV (254 nm, intensity = 21 mW cm^{-2}) in 4 h; and when tested in a two-step mode, i.e., batch adsorption and subsequent photodegradation, Fe–BiOCl/CS mineralized 65.34% of PFOS that was pre-concentrated in the solid phase under otherwise identical conditions; while the total degradation percentages of PFOS were 83.48% and 80.50%, respectively, for the two experimental modes. The photoactivated electrons and/or hydrated electrons and superoxide radicals primarily initiated the desulfonation of PFOS followed by decarboxylation and defluorination, through a stepwise chain-subsiding mechanism. The elevated photocatalytic

* Corresponding author.
E-mail addresses: rrather@sdsu.edu (R.A. Rather), dzhao2@sdsu.edu (D. Zhao).

https://doi.org/10.1016/j.chemosphere.2023.140585
Received 25 June 2023; Received in revised form 25 September 2023; Accepted 27 October 2023
Available online 28 October 2023

activity can be attributed to the effective separation of e^-/h^+ pairs facilitated by the (110) interlayer electrostatic field, Fe doping, and the presence of oxygen vacancies. This work reveals the potential of carbon-modified and Fe-co-catalyzed BiOCl for concentrating and degrading PFOS and possibly other persistent organic pollutants.

1. Introduction

Per and poly-fluoroalkyl substances (PFAS) have been widely used in industrial processes and domestic products since 1940s (Glüge et al., 2020; Leeson et al., 2021). As a result, PFAS have been detected in various water bodies including drinking water sources. An investigation by the US Geological Survey (USGS) and the Environmental Protection Agency (EPA) on 25 drinking water systems confirmed the presence of 2–12 PFAS, with concentrations ranging from 1 ng L^{-1} to 1102 ng L^{-1} in treated drinking water with an average concentration of 19.5 ng L^{-1} (Boone et al., 2019). Due to their extremely high chemical stability and the C–F bond energy (544 kJ mol^{-1}), the long half-life, bioaccumulation, and multiple adverse health impacts, PFAS contamination of drinking water has emerged as a major environmental concern (McCarthy et al., 2017; Dean et al., 2020). To mitigate human exposure, on March 14, 2023, EPA proposed the first-ever National Primary Drinking Water Regulation (NPDWR) for six priority PFAS including perfluorooctanoic acid (PFOA), perfluorooctane sulfonic acid (PFOS), perfluorononanoic acid (PFNA), hexafluoropropylene oxide dimer acid (HFPO-DA, commonly known as GenX Chemicals), perfluorohexane sulfonic acid (PFHxS), and perfluorobutane sulfonic acid (PFBS).

Of particular concern are two legacy long-chain PFAS, i.e., PFOS ($C_8HF_{17}O_3S$) and PFOA ($C_8HF_{15}O_2$). Although the industries in Europe and Northern America volunteered to phase out PFOS and PFOA in the early 2000s, the past applications resulted in widespread contamination of the aquatic systems including many drinking water sources. As the associated health effect data continue to mount, the US EPA proposed a maximum contaminant level of 4.0 ppt (ng L^{-1}) for PFOS and PFOA individually, which is much more stringent than the EPA's prior advisory level of 70 ppt with PFOS and PFOA combined (Gao et al., 2020; Zhang et al., 2019b).

PFAS are resistant to various natural and engineered degradation processes such as the standard biological and physical-chemical treatment (Kucharzyk et al., 2017), and numerous conventional and non-conventional technologies have been investigated to remove or degrade PFAS in water, including incineration (Longendyke et al., 2022), activated carbon (AC) adsorption (Lei et al., 2023), ion exchange (Fang et al., 2023), electrochemical degradation (Mirabediny et al., 2023), and advanced reduction and oxidation processes (Leonello et al., 2021). Among the most commonly used technologies are adsorption, ion exchange, and advanced oxidation processes. While adsorption by AC and ion exchange are rather mature technologies for removing organic pollutants from water, they do not degrade PFAS, and moreover, the regeneration of PFAS-laden AC or resins is rather challenging and often requires toxic and costly organic solvents such as methanol.

Advanced reduction/oxidation processes can degrade and mineralize (or defluorinate) PFAS, though the effectiveness varies. In recent years, photocatalytic degradation of PFAS has attracted growing interest for their low cost and relatively high degradation efficiency. To this end, various photocatalysts have been developed, such as TiO_2 (Furtado et al., 2021), In_2O_3 (Liu et al., 2021), and ZnO (Dehghani et al., 2022). However, conventional semiconductor-based photocatalysts bear some critical limitations, including 1) insufficient charge excitation and transfer ability, 2) insufficient redox potential at the active sites to degrade PFAS and generate reactive radical species (RRS), and 3) poor or unfavorable adsorption of PFAS. For instance, TiO_2 (P25) has been a classical photocatalyst, but it is not effective in degrading PFOA (Panchangam et al., 2009). Song et al. (2017) reported that TiO_2–P25 and In_2O_3 offered limited photocatalytic defluorination of PFOA due to improper valance band (VB) alignment that inhibited the formation of energetic holes, while Bismuth oxychloride (BiOCl) mineralized 59.3% of PFOA in 12 h, which was 1.7 and 14 times higher than TiO_2 and In_2O_3, respectively.

BiOCl has a layered lattice structure with an indirect band gap of ~3.3 eV, and it has a covalently and electrostatically coordinated crystal structure with four oxygen (O) and chlorine (Cl) atoms arranged in a decahedron shape (Lei et al., 2009). The coordination bonds (Bi–O and Bi–Cl) lead to the development of two indexed facets linked by sharing a common Cl–O edge (Keramidas et al., 1993). Furthermore, the strong electric fields between the layers facilitate the crystal growth in some suitable planes, i.e., (001), (101), and (110). In addition, the charge fields promote the transfer and collection of electrons through a photocatalytic excitation process (Lin et al., 2006). BiOCl has shown some promising activity for charge transfer and generation of RRS, which lead to various photocatalytic reactions, such as hydrogen production (Ye et al., 2015), N_2 conversion (Shen et al., 2021), and degradation of organic contaminants in water (Chen et al., 2010). Moreover, BiOCl has shown specificity for the removal of longer-chain PFAS through diverse mechanisms (Wu et al., 2021). Chen et al. (2022) reported that the exposed facet of BiOCl and the presence of oxygen vacancies enhanced the charge collection and separation in a photocatalytic degradation process. Similarly, Song et al. (2017) reported the oxygen vacancies in BiOCl facilitated the degradation of PFOA through a direct oxygen vacancy hole transfer mechanism. Yet, conventional BiOCl offers only limited degradation and defluorination for PFAS due to its unfavorable interactions between the material and PFAS (anions) and fast recombination of e^-/h^+. In addition, the current practice in photocatalytic degradation of PFAS involves the addition of photosensitizers into, and shooting light towards, the bulk water, which has a large volume but contains very low concentrations of PFAS (ng-μg L^{-1}). Such direct treatment of bulk water is not only inefficient, but also less effective for the mineralization of PFAS.

To overcome the drawbacks of the conventional single-phased photocatalysts, various composite photocatalytic materials have been reported to enhance the structural, surface, and chemical properties, such as Fe/TNTs@AC, BiOX/TiO_2, TiO_2/WO_3, and $Bi_3O(OH)(PO_4)_2$ (Li et al., 2020; Qanbarzadeh et al., 2020; Lashuk et al., 2022; Liu et al., 2022). Modification with carbonaceous materials has been found effective in enhancing the adsorption and photocatalytic activity of bismuth-based photocatalysts. For example, Xu et al. (2020) reported that BiOHP hybridized with microscale carbon spheres showing enhanced photocatalytic degradation of PFOA (up to 90%, c.f., 10% with neat BiOHP). Another effective strategy is to dope or deposit a metal such as Fe, Bi, or In to form a heterostructure, which may promote the interfacial charge transfer, leading to improved lifetime of the e^-/h^+ pairs and enhanced photocatalytic activity as the dopant metal modulates the band gap and also acts as a co-catalyst. Based on prior work by our group (Li et al., 2020) and others (Zhang et al., 2019a), we chose Fe as the dopant for BiOCl in this study. In addition to the cost-effectiveness and non-toxicity, Fe doping can also regulate the catalytic properties in several ways: 1) it can strongly influence the optoelectronic properties of the Fe–BiOCl system after the Fermi level equilibration; 2) Fe doped in the lattices of host BiOCl creates localized energy states within the band gap, which can served as electron traps, whereas Fe grafted on the surface of BiOCl can promote charge separation through band bending and the creation of a Schottky barrier at the heterojunction; and 3) Fe-doping can also alter the band gap, resulting in enhanced absorption of light. Zhang et al. (2019a) reported that Fe doping of BiOCl nanosheets enhanced its light absorption ability and the lifetime of the photoexcited charge carriers.

In terms of treatment configuration, the conventional practice in photocatalytic processes has been involving the addition of photosensitizers into, and shooting light towards, the bulk water (aqueous phase). However, this approach may not be suitable for treating a large volume of water contaminated with trace concentrations of PFAS (ng-μg L^{-1}) because of the poor energy efficiency and the side effects associated with the chemical addition (including requirement of extreme pH). To this end, solid-phase photocatalysis may offer some advantages, where PFAS are first adsorbed/concentrated on a small volume of an adsorptive photocatalyst from bulk water, and then photodegraded. Moreover, thanks to the small volume, this method also allows for employing additional engineered means (e.g., use of photosensitizers or strong reductants/oxidants, and/or adjusting the temperature and pH) to enhance the photodegradation.

The goal of this study was to prepare and test a new type of carbon-modified Fe-doped heterostructure (Fe–BiOCl/CS) for enhanced degradation of PFOS. The specific objectives were to: 1) prepare Fe–BiOCl/CS through a facile hydrothermal process, 2) optimize the Fe loading on BiOCl/CS, 3) characterize Fe–BiOCl/CS through various optical, morphological, and surface analysis techniques, 4) test adsorption rate and capacity of Fe–BiOCl/CS for PFOS, 5) determine the photocatalytic degradation kinetics, and 6) elucidate the photodegradation mechanisms based on material characterization, radical scavenging tests, electron paramagnetic resonance (EPR) spectroscopy analysis, and intermediate products.

2. Experimental

2.1. Chemicals and reagents

Bismuth nitrate pentahydrate ($Bi(NO_3)_3.\ 5H_2O$, Alfa Aesar 98%), ferric nitrate nonahydrate ($Fe(NO_3)_3.\ 9H_2O$, Fischer Scientific, 99%), D-glucose anhydrous ($C_6H_{12}O_6$, Alfa Aesar, 98%), ethylene glycol ($C_2H_6O_2$, VWR, high purity grade), potassium chloride (KCl, BDH VWR, 99%), sodium hydroxide (NaOH, ACS grade, Thermos Scientific), 1,4, benzoquinone (BZQ, 97%, TCL), perfluorooctane sulfonate (PFOS, Sigma Aldrich, >98%), Sodium perfluoro-1-[$^{13}C_8$] octane sulfonate (M8PFOS, Wellington labs Inc. >99%) were used as received. Other basic chemicals such as isopropyl alcohol (IPA, 99.5%, SEMI grade), ethanol (EtOH, 70%, biotechnology grade), and potassium iodide (KI, 99%, ACS grade) were purchased from VWR International (USA). All solutions and reagents were prepared in deionized water (>18 MΩ cm).

2.2. Synthesis of Fe–BiOCl/CS

Fe–BiOCl/CS was prepared by a facile chemical-hydrothermal method using bismuth nitrate ($Bi(NO_3)_3$), ferric nitrate nonahydrate ($Fe(NO_3)_3\ \cdot 9H_2O$), and D-glucose ($C_6H_{12}O_6$) as precursors. As shown schematically in Fig. S1 of the Supporting Information (**SI**), 1.579 g (4 mmol) of $Bi(NO_3)_3$ and 0.028 g of $Fe(NO_3)_3$ were dissolved in 25 mL ethylene glycol and stirred for 30 min. Meanwhile, in another flask, 0.298 g (4 mmol) of KCl and 0.154 g of D-glucose were dissolved in 25 mL water under constant stirring (30 min). The two solutions were instantly mixed, forming a milky white precipitate, and the mixture was further stirred at room temperature for 30 min. Subsequently, the mixture was diluted with 20 mL H_2O and transferred into a Teflon-lined autoclave (100 mL), and hydrothermally treated at 160 °C for 24 h. The final product was harvested by centrifugation and thoroughly washed with ethanol and water. The resulting dark-grey powder (Fig. S2) was dried at 80–90 °C overnight, and then calcined in a tube furnace at 300 °C under N_2 atmosphere for 3 h. For comparison, the relevant base materials including BiOCl, Fe–BiOCl, and BiOCl/CS were also prepared through the same procedure.

2.3. Characterization of the photocatalysts

The morphological characteristics were revealed using a JEOL JEM-2100F transmission electron microscope (TEM) and a JEOL JEM-7600F scanning electron microscope (SEM). The crystal structure was analyzed using a Bruker D2 Phaser x-ray diffractometer (Germany), with Cu-Kα radiation (40 kv, 30 mA, $\lambda = 1.54\ A^o$) and a scanning range of 10-80° with a step size of 10° min^{-1}. The surface chemical states and elemental composition were determined by X-ray photoelectron spectroscopy (XPS, Kratos) with the Al-Kα as the source operated at 15 kV. The structural characteristics were studied by Raman spectroscopy (Horiba, LabRAM, Japan) with a He–Ne laser (5 mW) and 532 nm excitation. The optical properties were examined using a Thermo Scientific Nicolet iS20 Fourier transform infrared (FTIR) spectrometer with a resolution of 4 cm^{-1} at 32 scans in the transmission mode. Specific surface area and porosity were determined by a Micromeritics BET surface area analyzer. Zeta potential (ξ) was measured by a Nano-ZS90 Zetasizer (Malvern, UK). In addition, electron paramagnetic resonance spectroscopy (EPR, Bruker EPR, A300) analyses were conducted to assess superoxide radicals ($O_2^{\bullet-}$) generated during the reaction, with 5,5-dimethylpyroline-N-oxide (DMPO) as the $O_2^{\bullet-}$ trapping agent.

2.4. Adsorption kinetic and isotherm tests

The adsorption kinetic and isotherm tests were conducted in the dark using 40 mL high-density polyethylene (HDPE) vials. The adsorption was initiated by mixing a PFOS solution (100 μg L^{-1}, 40 mL) with 0.12 g of a catalyst at pH 4.3 (±0.2) on a rotator (80 rpm). At pre-determined times, the solid particles were separated by centrifugation (3000 RPM, 3 min), and the supernatant was analyzed for PFOS remaining in the solution. The adsorption isotherm tests were performed following the same experimental procedure, with the initial PFOS concentration varied between 0.1 and 8 mgL^{-1} and at a fixed material dosage of 1 g L^{-1} and an equilibration time of 12 h. All tests were conducted in duplicate.

2.5. Photocatalytic degradation of PFOS

The photocatalytic degradation experiments were conducted in two different approaches. The first approach was to directly photodegrade PFOS in the aqueous solution. To this end, a mixture of 10 mL aqueous solution containing PFOS (100 μg L^{-1}) and 0.01 g of a photocatalyst in a quartz reactor was irradiated in a UV reactor (21 mW cm^{-2}, 254 nm, Rayonet, Southern New England UV Co., Bradford) for 4 h with intermittent shaking. The resulting aliquots were sampled, filtered (0.22 μm polyether sulfone, PES), and analyzed for fluoride (F^-). The second approach followed a two-step concentrate-and-degrade process, namely, adsorption of PFOS on Fe–BiOCl/CS and then irradiate the PFOS-laden solids in the same UV reactor. In this regard, PFOS was preloaded on the solids via the batch adsorption for 6 h (PFOS = 100 μg L^{-1}, volume = 40 mL, and material dosage = 3 g L^{-1}). The adsorption was able to pre-concentrate 83.6% of the aqueous-phase PFOS onto the solid phase. Upon equilibrium, the solid particles were allowed to settle by gravity and the supernatant (~95%) was pipetted off. The solids were then transferred into a quartz reactor with the subsequent addition of 7–8 mL of deionized water to give a total volume of 10 mL. The mixture was then irradiated in the UV reactor for 4 h, and then the defluorination was measured by analyzing the fluoride ion in the solution phase. In addition, the solids were extracted using methanol (40 mL) at 80 °C for 12 h to quantify PFOS remaining in the solid phase.

To probe the roles of electrons, holes, and radicals in the PFOS defluorination, the photocatalytic degradation experiments were carried out in the presence of 10 mM of a scavenger. The scavengers included silver nitrate ($AgNO_3$), p-benzoquinone (p-BZQ), and 2Na-ethylenediamine tetraacetic acid (EDTA) for scavenging of electrons, $O_2^{\bullet-}$, and h^+, respectively.

The gauge the reactive life and reusability, the same Fe–BiOCl/CS

composite was used in four consecutive cycles following the aqueous photodegradation protocol, where Fe–BiOCl/CS was harvested after each cycle by centrifugation followed by washing cycles with water.

2.6. Chemical analysis

PFOS in solution and the reaction intermediates were analyzed using an ultra-performance liquid chromatography system coupled with an orbitrap mass spectrometer (UPLC-EXPLORIS/MS) with heated electrospray ionization (ESI). A C18 column (Luna, 3 μm, 100 A°, 2 × 50 mm) was employed as the stationary phase. The mobile phase consisted of solution A (2 mM ammonium acetate in DI water) and solution B (acetonitrile 100%), and the flow rate was 200 μL/min. The detection limit of the instrument was 1 μg L^{-1}, M8PFOS (sodium perfluoro [$^{8}C_{13}$] octane sulfonate) was used as an internal standard for the analysis. Aqueous F^- was quantified by ion chromatography (Dionex, USA) with a Dionex Ionpac AS22 column and a mixture of sodium carbonate (4.5 mM) and bicarbonate (1.4 mM) as the eluent at a flow rate of 1.2 mL/min. The instrument detection limit was ~10 μg L^{-1}.

3. Results and discussion

3.1. Characterization of Fe–BiOCl/CS

Fig. 1a shows the XRD pattern of Fe–BiOCl/CS along with pristine BiOCl, Fe–BiOCl, and BiOCl/CS. The diffraction peaks in pristine BiOCl indicate a typical bismoclite phase (ICDS-06-0249), with a tetragonal crystal structure (a = 3.89, b = 3.89, and c = 7.36). The peaks at 11.98°, 25.86°, 32.49°, and 33.44° are assigned to (110), (001), (101), and (102) planes, respectively. The similarity between the XRD spectra of BiOCl and Fe–BiOCl can be attributed to 1) the small fraction of Fe (<1%) in the Fe–BiOCl composite, which was not enough to alter the crystal structure of BiOCl, and 2) the Fe-phase was amorphous. After carbon modification and Fe loading, the growth of (001) and (102) planes was slightly reduced in Fe–BiOCl/CS due to the addition of D-glucose, which acted as both a carbon source and a shape-directing agent (Rather et al., 2019). The growth inhibition was also observed in the high-angle annular dark field scanning (HAADF/STEM) micrographs. BiOCl sheets with variable sizes and growth were observed in all cases. The average size (i.e., the side length of square sheets) of the pristine BiOCl sheets was 406 nm (Fig. 1b), which was decreased to 178 nm after the addition of D-glucose or carbon modification in BiOCl/CS (Fig. 1c) and Fe–BiOCl/CS (Fig. 1d). However, the size of Fe–BiOCl particles was similar to pristine BiOCl (Fig. 1e), confirming the role of D-glucose as a growth-controlling and shape-directing agent. In addition, some rod-shaped particles (125 nm) were observed in BiOCl/CS and Fe–BiOCl/CS due to the D-glucose stabilization effect. Modification with carbon derived from D-glucose increased the overall specific surface area (from 10.65 to 15.55 m^2g^{-1}) and pore volume (from 0.04 to 0.13 cm^3g^{-1}) of Fe–BiOCl/CS (Fig. S3, Table S1), which in turn can enhance the adsorption capacity for PFOS (Wang et al., 2012; Xu et al., 2020). Furthermore, the decrease in the sheet size also facilitates light-induced charge transfer and collection on the surface, which directly inhibits the rate of e^-/h^+ pair recombination (Aprile et al., 2008).

The HRTEM images (Fig. 2a-d) align with the HAADF/STEM images (Fig. 1b–e). The lattice spacing of 0.27 nm corresponds to the (110) plane (Fig. 2e) of BiOCl, which is the primary and highly exposed facet. These exposed facets (110) effectively separate the excited e^-/h^+ pairs due to the interlayer electrostatic interaction between negatively charge Bi–O and positively charged Bi–Cl layers (Wang et al., 2019), thus enhancing their lifetime. Additionally, the lattice spacing of 0.34 nm was attributed to (101) plane of the rod morphology (Fig. 2f) of Fe–BiOCl/CS. The EDS elemental mapping (Fig. 2g–l) shows homogenous and uniform distribution of all elements and confirms the successful loading of Fe on the Fe–BiOCl/CS composite.

The crystallinity, molecular interactions, defects, and nature of grafted carbon in the Fe–BiOCl/CS heterostructure were further analyzed with Raman and infrared spectroscopy. Fig. 3a shows the typical vibrations in the Raman spectra of BiOCl, BiOCl/CS, and Fe–BiOCl/CS. An intense band for the Bi–Cl (A_{1g}) internal stretching vibration was recorded at 143.36 cm^{-1} for all samples confirming the formation of BiOCl crystal without any structural defects. The small peak at 395.5 cm^{-1} is ascribed to the B_{1g} and E_g bands originating from vibrations of O atoms (Cao et al., 2009). However, after the carbon modification (BiOCl/CS and Fe–BiOCl/CS), two peaks at 1362.5 cm^{-1} and 1576.20 cm^{-1} emerged, which are assigned to the structural defect band (D band) and primary graphite band (G band) of sp^2 carbon (Yu et al., 2018), respectively. In addition, a 2D band was also observed at 2761.55 cm^{-1}, confirming the small thickness of grafted carbon layers and indicating its graphitic nature (Shearer et al., 2016). The peaks between 400 and 700 cm^{-1} correspond to the Fe–O stretching bands, i.e., Fe–O symmetric bending at 421.28 cm^{-1}, Fe–O symmetric stretching at 514.96 cm^{-1}, and Fe–O symmetric stretching at 693.59 cm^{-1}, the increase in the band intensity confirmed the presence of the Fe

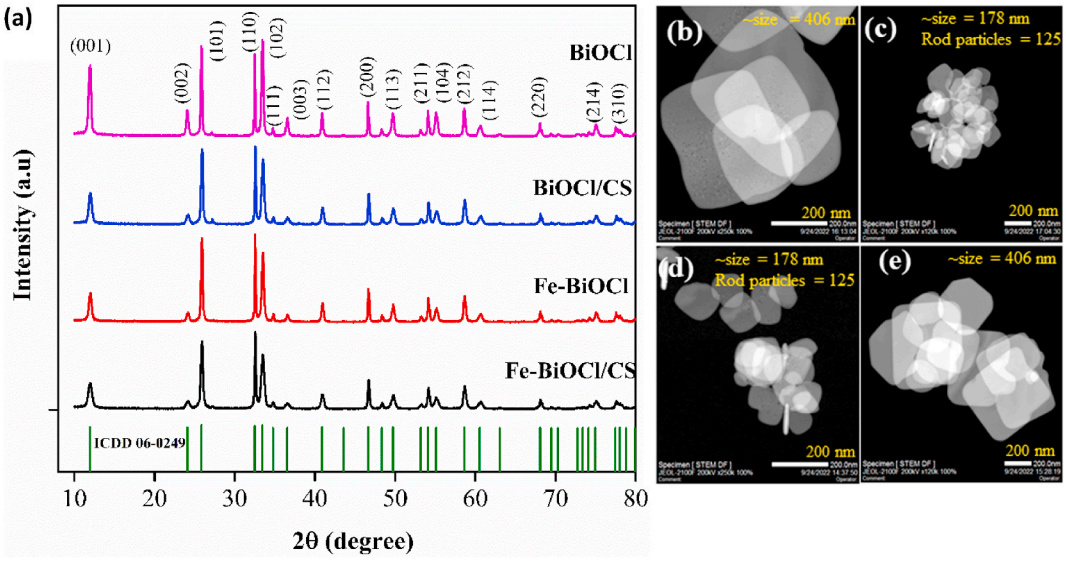

Fig. 1. (a) X-ray diffraction pattern of various photocatalysts, and the HAADF/STEM images of (b) pristine BiOCl (c) BiOCl/CS (d) Fe–BiOCl/CS and (e) Fe–BiOCl. All samples were calcined at 300 °C for 3 h.

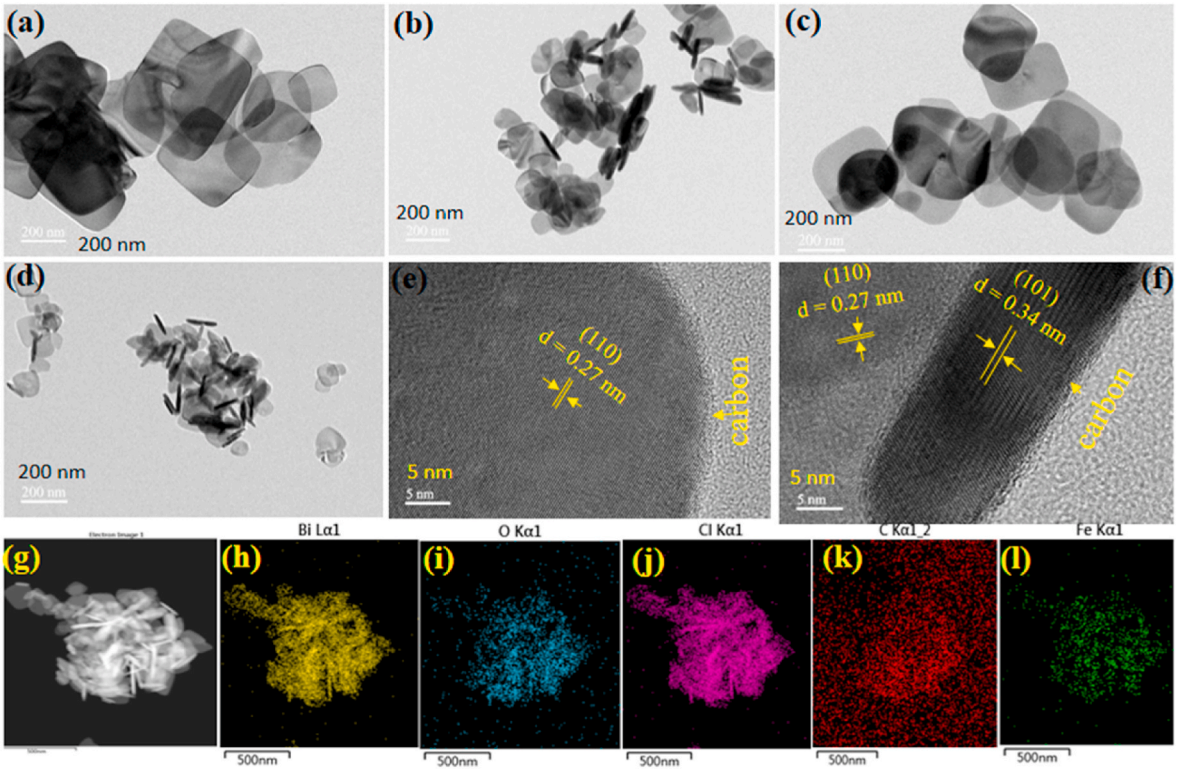

Fig. 2. High resolution transmission electron microscopic (HRTEM) images of (a) pristine BiOCl, (b) BiOCl-CS, (c) Fe–BiOCl, and (d) Fe–BiOCl/CS, (e–f) lattice fringes in Fe–BiOCl/CS displaying the d-spacing of respective planes, and (g) micrograph selected for elemental mapping and mapping patterns of (h) Bi, (i) O, (j) Cl, (k) C, and (l) Fe.

functionalities in Fe–BiOCl/CS. The vibrational bands of Fe–O were also detected in the FTIR analysis (Fig. S4), where the bands at 621.8 cm^{-1} and 473 cm^{-1} correspond to the Fe–O stretching mode and Fe–O bending vibration mode, respectively, and the intensity for both bands increased in Fe–BiOCl and Fe–BiOCl/CS.

The carbon modification was further confirmed by FTIR analysis of Fe–BiOCl/CS (Fig. 3b), where an increase in the magnitude of the vibrational band at 1127.5 cm^{-1} was observed, which can be attributed to the C–O stretching (Yin et al., 2022). The carbon modification was expected to help (1) increase the adsorption capacity of BiOCl for PFOS through hydrophobic interactions and (2) increase the electron mobility due to the graphitic nature of the carbon, thus enhancing the photocatalytic degradation of PFOS.

The surface chemical states of individual constituents were analyzed by XPS, and signals were attained for all individual elements (Bi, O, Cl, C, and Fe) in Fe–BiOCl/CS (Fig. S5). The deconvoluted spectra of Bi (Fig. 3c) showed two typical spin-orbital states at 159.3 eV (Bi $4f_{7/2}$) and 164.5 eV (Bi $4f_{5/2}$) corresponding to the Bi^{+3} oxidation state (Zou et al., 2019). The peaks in the oxygen scan (Fig. 3d) at 530.0 and 533.1 eV are assigned to Bi–O and C–OH bindings, whereas that at 531.7 eV is due to the hydroxyl group and the presence of oxygen vacancies in the lattice structure (Morgan, 2023; Niu et al., 2020; Zhang et al., 2022). The carbon (Fig. S6a) spectra were deconvoluted into three peaks at binding energies 284.7 eV, 286.2 eV, and 288.6 eV, which are assigned to C–C, C–O, and C=O, respectively. These data further confirm the interactions between carbon and the Bi–O layer of the crystal lattice. For Cl (Fig. S6b), the two peaks at 197.9 eV and 199.5 eV are assigned to Cl $2p_{3/2}$ and Cl $2p_{1/2}$ spin states due to ionic and covalent interactions of Cl with Bi or Oxygen. Moreover, in the Fe 2p scan (Fig. S6c), two small peaks were detected at 705.8 eV and 724.64 eV ascribed to the metallic state Fe^0 (Wang et al., 2010) and Fe^{+3} state of iron oxide (Tariq et al., 2018). The metallic iron resulted from the reduction of ferric iron in the presence of D-glucose and under the elevated hydrothermal conditions (Rather et al., 2017).

3.2. Photocatalytic degradation of PFOS by directly irradiating solution/photocatalyst mixtures

The photocatalytic performance of Fe–BiOCl/CS was first investigated under 254 nm UV light irradiation and by directly treating the PFOS solution without the pre-adsorption stage. The band gap of BiOCl sheets usually straddles around 3.1–3.3 eV (Wu et al., 2021). Fe was selected as a co-catalytic material because it showed greater enhancement of the defluorination activity during PFOS degradation compared to Ce, Ga, and Al (Fig. S7). The Fe loading amount was optimized by varying the molar ratios of $Fe(NO_3)_3$ to $Bi(NO_3)_3$. As shown in Fig. 4a, the highest defluorination activity (83.0%) was observed at the Fe:Bi molar ratio of 0.07:4, or 0.92% of atomic weight Fe on the surface (Table S2). Excessive Fe (>1.8 wt%) may induce lattice disorder and act as recombination centers of the charge carriers and decrease specific surface area and pore size (Yu et al., 2014; Zhu et al., 2021). Furthermore, the final defluorination percentage of Fe–BiOCl/CS was >2 folds that of pristine BiOCl (Fig. 4b), signifying the roles of the surface modification in facilitating the charge transfer and boosting the photocatalytic activity. Based on the 5-h defluorination kinetic data (Fig. 4b), the photoactivity of the materials followed the order of: Fe–BiOCl/CS (88.51%) > Fe–BiOCl (68.68%) > BiOCl/CS (53.91%) > BiOCl (40.63%).

For Fe–BiOCl/CS the total degradation efficiency achieved in 4 h UV irradiation was of 83.48%, the linear kinetic profile of PFOS photodegradation (Fig. 4c) for Fe–BiOCl/CS suggested a pseudo-first order kinetics (Eq. (1)) with a rate constant of 0.40 h^{-1} ($R^2 = 0.9071$).

$$kt = lnC/C_0 \quad (1)$$

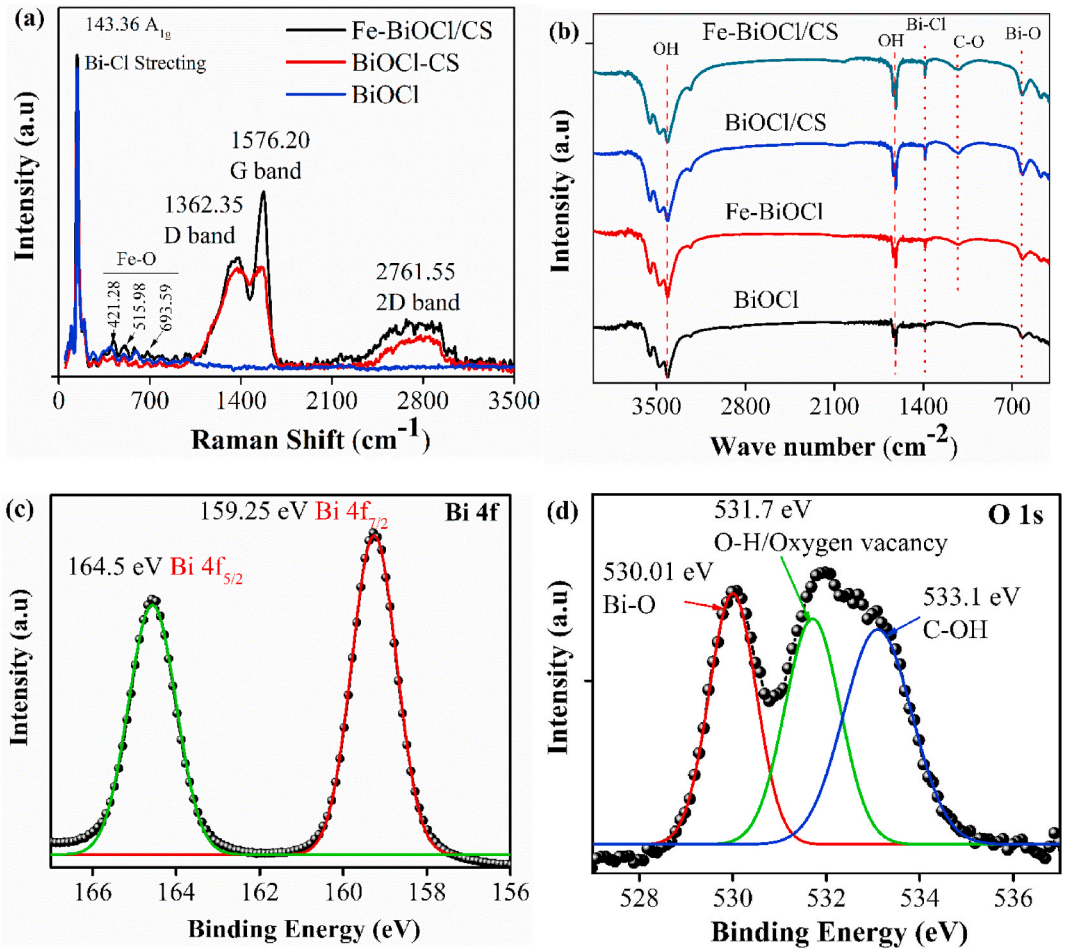

Fig. 3. (a) Raman and (b) FTIR spectra of BiOCl, Fe–BiOCl, BiOCl/CS, and Fe–BiOCl/CS. High resolution XPS spectra of Fe–BiOCl/CS displaying individual deconvoluted peaks of (c) Bi 4f and (d) O 1s.

3.3. Solid-phase photocatalytic degradation of PFOS pre-adsorbed on Fe–BiOCl/CS

While the foregoing results indicated the effective photocatalytic activity of Fe–BiOCl/CS for PFOS, the adsorptive nature of the composite material may enable a concentrate-&-destroy treatment strategy, which can be more cost-effective for treating trace levels of PFAS in large volumes of water. To this end, the same material was further tested in a two-step process, i.e., adsorption of aqueous PFOS on Fe–BiOCl/CS, and then photodegradation of the adsorbed PFOS by irradiating the PFOS-laden solid particles.

Fig. 5a shows the adsorption kinetics of PFOS by Fe–BiOCl/CS. At a dosage of 3 g L^{-1}, more than 77.2% of the initial PFOS (100 μg L^{-1}) was adsorbed within 10 min and the equilibrium was reached after 6 h with 83.63% uptake of the initial PFOS. The rapid adsorption rate can be attributed to several factors, such as the crystalline sheet structure of Fe–BiOCl/CS, large pore size (Xiong et al., 2011). Furthermore, the apparent type IV BET isotherm (Fig. S3) and the relatively high surface area and porosity also contribute to the higher adsorption efficiency of Fe–BiOCl/CS than the other materials. Fig. 5b presents the adsorption isotherm of PFOS by Fe–BiOCl/CS. The experimental data were interpreted using the classical Langmuir model,

$$q_e = \frac{bQ_{max}C_e}{1 + bC_e} \quad (2)$$

where q_e is the equilibrium uptake of PFOS, C_e is the corresponding aqueous-phase PFOS concentration, Q_{max} is the maximum Langmuir adsorption capacity, and b is the Langmuir affinity constant. Fe–BiOCl/CS offered a Q_{max} of 1.51 mg/g for PFOS with a b value of 4.10 L mg^{-1}.

The pH at point of zero charge (pH_{pzc}) of Fe–BiOCl/CS was measured to be 4.79 through the zeta potential analysis (Fig. S8). The photocatalytic defluorination performance of Fe–BiOCl/CS was investigated under different pH conditions (Fig. S9), including pH 4.75 (pzc), pH 4.3 (positive surface charge), and pH 5.3 (negative surface charge). Notably, the highest defluorination activity (65.34%) was observed at pH 4.3 following the two-step adsorption and photo-defluorination procedure. The higher defluorination at the lower pH is attributed to the more favorable electrostatic interaction between the PFOS anions and Fe–BiOCl/CS surface. Therefore, the pH at the adsorption stage was maintained at 4.3 (±0.2) to enhance the adsorption and the subsequent defluorination.

Fig. 5c shows the effect of material dosage in the adsorption stage on the defluorination of PFOS. The highest defluorination (65.34% of fluorine pre-adsorbed) was observed at a dosage of 3 g L^{-1}, which is 2 times higher than that (31.27%) at a dosage of 1 g L^{-1}. At 3 g L^{-1}, 80.5% of the total pre-adsorbed PFOS was photodegraded after 4 h of UV irradiation (Fig. 5d). At a higher dosage, PFOS molecules are more likely to be adsorbed on the shallow surface sites that are more photo-accessible, and thus more prone to attacking by the photo-generated charge carriers (Zhu et al., 2021). However, excessive particles in a given volume of solution may block the UV light, and thus lower the defluorination rate.

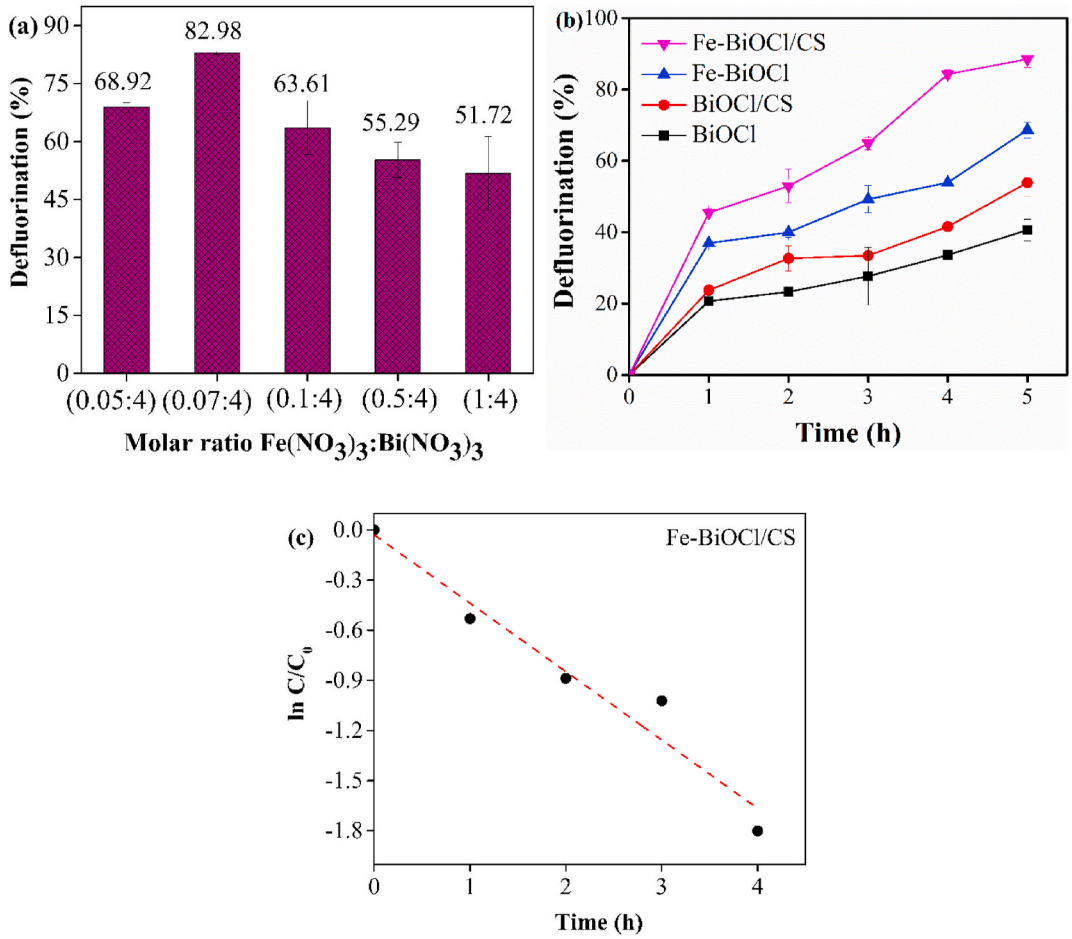

Fig. 4. (a) Effect of Fe at different Fe:Bi molar ratios on the defluorination of PFOS by Fe–BiOCl/CS after 4-h UV irradiation, (b) Defluorination kinetics of PFOS by four different photocatalysts, irradiation time (5 h) (c) Linearized plot of the photodegradation kinetic data of PFOS by Fe–BiOCl/CS. Experimental conditions: Initial PFOS = 100 μg L^{-1}, material dosage = 1 g L^{-1}, irradiation time = 4 h, pH = 5.33 ± 0.2, UV intensity = 21 mW cm^{-2}, wavelength = 254 nm. The experiments were carried out by directly irradiating the solution/material mixture without the pre-adsorption stage.

3.4. Reusability of Fe–BiOCl/CS

Fig. S10 shows the preliminary testing data on the reusability of Fe–BiOCl/CS under direct photocatalytic degradation conditions (i.e., without the pre-adsorption). No significant change was observed between the first two runs, whereas the defluorination level decreased to 66. 43% after the 4th run. The decrease in the photocatalytic performance can be ascribed to 1) accumulation of some shorter-chain PFAS intermediates during the preceding cycles of reactions on the surface of Fe–BiOCl/CS, which may block the access of the photoactive sites and/or compete for the reactive species (Zhu et al., 2021), and 2) partial distortion of the BiOCl/CS heterostructure.

The high-resolution XPS analysis of the reused Fe–BiOCl/CS (Fig. S11) revealed that while the chemical states of all the elements remained intact, the intensity of the peak corresponding to the oxygen vacancies (shifted from 531.70 to 530.16 eV) decreased, which is associated with the adsorption of molecular oxygen on Fe–BiOCl/CS, leading to the formation of superoxide radicals, which played an important role in the PFOS degradation (Section 3.5). This observation supports the presence of the oxygen vacancies. Moreover, a small shift in the peaks of C1s was observed, i.e., C–C (284.7–284.6 eV), C–O (286.2–286.1) and C=O (288.6–288.3 eV), due to interactions with the adsorbed PFOS as it changes the electronic environment of carbon. The XPS data further revealed an insignificant change in the weight percentage of all elements after reuse in Fe–BiOCl/CS (Tables S2 and S3), e.g., the change in the atomic ratio of Fe was ~0.06% (0.92%–0.86%) (Fe leaching was less than 3%), showing its physical stability. Furthermore, SEM micrographs were taken for fresh and used Fe–BiOCl/CS. As shown in Fig. S12, these images can hardly tell notable morphological changes of the sheet-like heterostructure after the 4th cycle of reuse.

3.5. Degradation mechanism of PFOS by Fe–BiOCl/CS

$AgNO_3$ and p-benzoquinone have been commonly used as a scavenger for electrons and superoxide radicals, respectively. As shown in Fig. 6a, the presence of $AgNO_3$ and p-benzoquinone in the reaction mixture strongly quenched the defluorination of PFOS by Fe–BiOCl/CS, indicating the important roles of e^- and $O_2^{\bullet-}$. Furthermore, the effective production of superoxide radicals was confirmed by EPR spectroscopy using 5,5, dimethylpyroline-N-oxide (DMPO) as a spin trapping agent, as it reacts with superoxide radical to produce a stable adduct known as DMPO-OOH. As shown in Fig. 6b, at time 0 and in the absence of UV light, no EPR signals were detected in the Fe–BiOCl/CS system, while at 10 min and in the presence of the UV light, strong signals corresponding to DMPO-OOH were detected, indicating the formation of $O_2^{\bullet-}$ radicals. The scavenger tests further confirmed the photocatalytic reductive degradation mechanism for the initial PFOS breakdown. The reductive degradation mechanism may be initiated in two different ways, (1) by aqueous/hydrated electron (e_{aq}) and/or (2) direct attack by superoxide radicals ($O_2^{\bullet-}$). The hydrated electrons possess high reactivity (E_o = −2.9 V) and reducibility and can effectively react with halogenated organic compounds including PFAS (Neta et al., 1988). Fluorine atoms

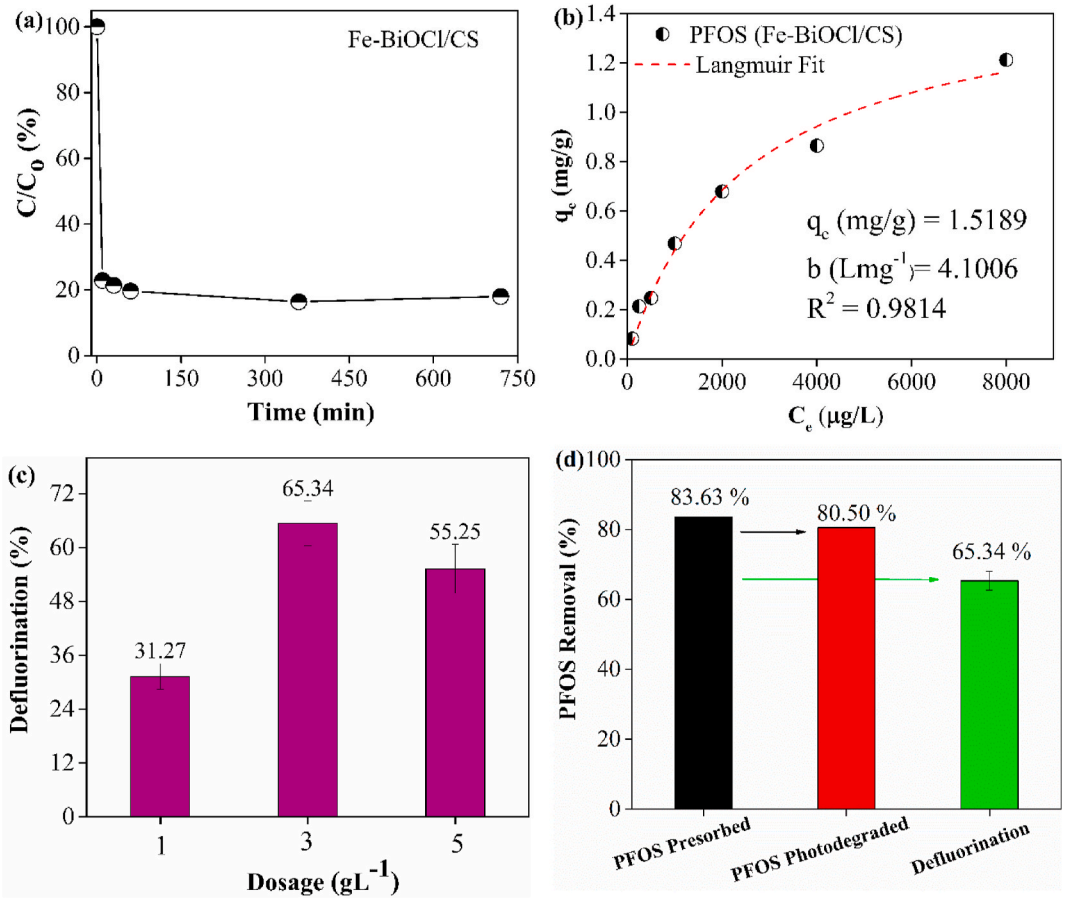

Fig. 5. (a) Adsorption kinetics of PFOS by Fe–BiOCl/CS (initial PFOS = 100 µg L^{-1}, catalyst dosage = 3 g L^{-1}, solution volume = 40 mL, pH = 4.3 ± 0.2, (b) Adsorption isotherm of PFOS with Fe–BiOCl/CS fitted with the Langmuir model (initial PFOS = 0.1–8 mg L^{-1}, material dosage = 1 g L^{-1}, pH = 4.3 ± 0.2, equilibrium time = 12 h), (c) Effect of catalyst dosage on the defluorination of PFOS. (Initial PFOS during adsorption = 100 µg L^{-1}, pH during photodegradation = 4.3 ± 0.2, irradiation time = 4 h, UV intensity = 21 mW cm^{-2}, UV wavelength = 254 nm), (d) PFOS adsorbed before photodegradation (based on total PFOS in the system) and photodegradation and defluorination of the pre-adsorbed PFOS (based on the mass of PFOS in the solid phase). Initial PFOS in adsorption tests = 100 µg L^{-1}.

in the PFOS may act as the primary reductive centers for the hydrated electrons initiated by the defluorination reaction through the nucleophilic attack on the PFAS chain. Huang et al. (2007) observed an increase in the rate constant with an increase in fluorocarbon chain length (or F number) in an e_{aq}-driven photodegradation reaction, demonstrating fluorine atoms as the reductive centers. Similarly, the generation of $O_2^{\bullet-}$ is primarily attributed to the reaction between the excited electrons and molecular oxygen. The reduction potential of $O_2^{\bullet-}$ in water is −0.16 V (Wood, 1988), which is strong enough to facilitate the nucleophilic attack on the PFOS chain. Moreover, the pH significantly affects the lifetime of $O_2^{\bullet-}$, which can be protonated to hydrogen peroxide (H_2O_2) under acidic conditions. At pH 4.3, the generation of H_2O_2 is possible, which can act as an oxidant to facilitate the degradation and mineralization process of PFOS.

No quenching in the overall photocatalytic activity was observed in the presence of EDTA, substantiating insignificant role of holes in the photodegradation of PFOS. In fact, the presence of EDTA increased the photodegradation of PFOS from 84.3% to 90.0%, suggesting that suppressing the holes may aid in the reductive degradation of PFOS.

Based on the experimental findings and relevant literature reports, Fig. 6c illustrates the mechanism and pathway of the photocatalytic degradation of PFOS by Fe–BiOCl/CS. First, the UV photonic influx excites the BiOCl component of the Fe–BiOCl/CS composite. UV–Vis absorption spectroscopy was employed to estimate the energy gaps (E_g) of different BiOCl based photocatalysts. As shown in Fig. S13a, neat BiOCl exhibited an E_g value of 3.26 eV, which was within the reported range (3.1–3.3 eV) (Bai et al., 2014). The E_g value was shifted to 2.93 eV upon the carbon modification (BiOCl/CS) (Fig. S13b) and 3.08 eV upon the incorporation of Fe^{+3} (Fe–BiOCl) (Fig. S13c). For Fe–BiOCl/CS, the E_g value was further narrowed to 2.83 eV. This variation is attributed to the alteration in the optoelectronic properties of Fe–BiOCl/CS. It was postulated that the modification with CS can lead to new electronic states within the band gap, whereas the incorporation of Fe^{+3} influenced the electronic properties of BiOCl by the Fermi level equilibration and creation of a charge separation barrier. These interactions among the constituent elements played a crucial role in charge separation after photoexcitation, leading to the higher efficiency for PFOS degradation and resulting in the e^-/h^+ pairs in their respective excited levels (Eq. (3)). As revealed by XPS analysis, being in Fe^0 and Fe^{+3} state, iron plays a role both as a co-catalyst and an electron carrier during the PFOS photodegradation. Fe^{+3} helps in the transportation of electrons by acting as a trap (Mi et al., 2016), thus promoting the separation of e^-/h^+ pair in Fe–BiOCl/CS. While at the Fe^0–BiOCl interface, a Schottky barrier is created (Yang et al., 2021) because the work function of Fe^0 is higher (4.5–4.7 eV) (Wilson, 1966) than that of Bi (4.2–4.3 eV) (Muntwiler and Zhu, 2008). Under UV irradiation, the electrons are transferred across the Schottky barrier, towards Fe^0 via the photo-induced charge transfer mechanisms, leading to the overall change in the electronic properties of the interface and facilitating the separation of electrons and holes. In the meantime, Fe^0 as a co-catalyst effectively injects these electrons into the anti-bonding orbital of molecular O_2, resulting in the formation of superoxide radicals (Eq. (4)). In addition, the oxygen vacancies on Fe–BiOCl/CS, as determined by the XPS analysis of oxygen O_{1s} (531.7 eV peak), act as the trap centers for

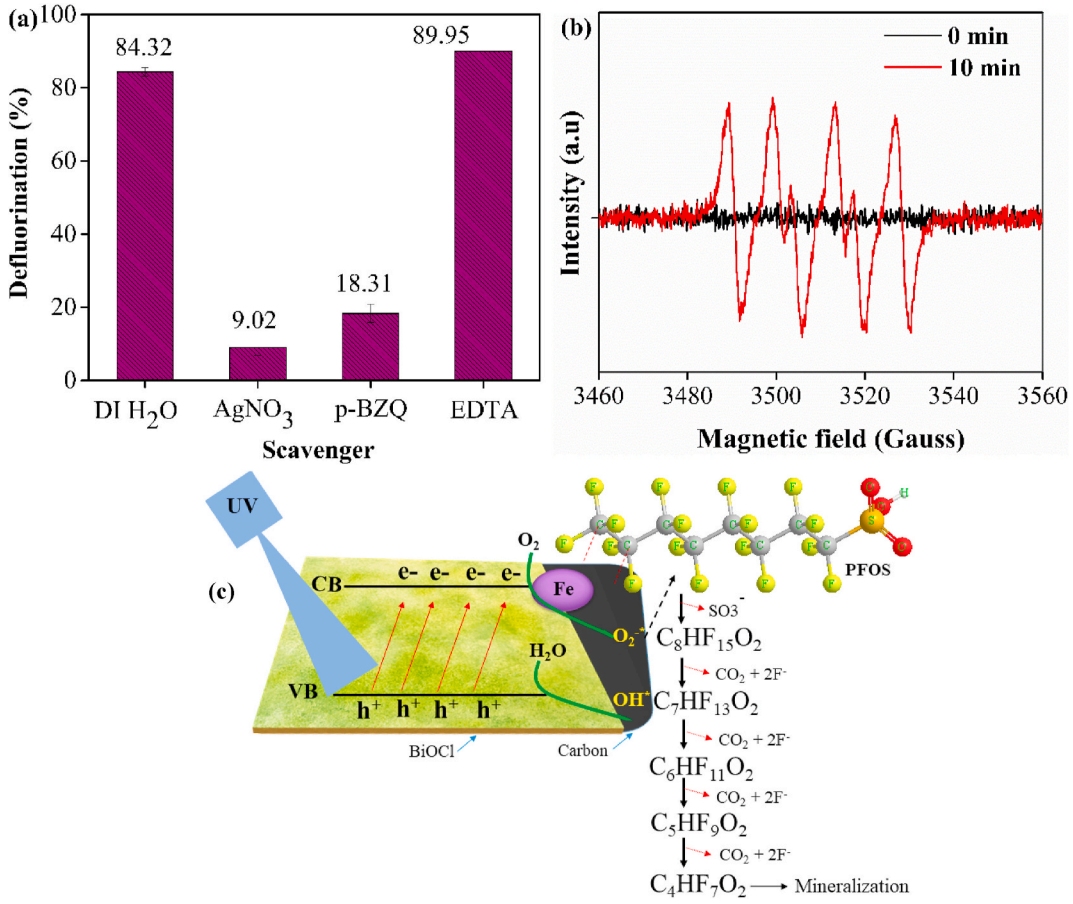

Fig. 6. (a) Effect of electrons and radical scavengers on the defluorination performance (concentration of each scavenger = 10 mM, PFOS = 100 μg L^{-1}, Dosage = 1 g L^{-1}, irradiation time = 4 h), (b) EPR study of Fe–BiOCl/CS at t = 0 and t = 10 min in presence of DMPO as superoxide radical scavenger and under UV irradiation, and (c) Proposed photodegradation mechanism and pathway of PFOS on Fe–BiOCl/CS under UV irradiation.

the excited electrons (Li et al., 2017). These oxygen vacancy based trap sites facilitate the transfer of electrons toward the adsorbed oxygen species, facilitating the formation of superoxide radicals. The resulting superoxide radicals can disproportionate at pH 4.3 to generate H_2O_2 (Eq. (5)) or initiate the degradation process by direct PFOS desulfonation (Eq. (7)). The excess electrons could be solvated in the form of hydrated aqueous electrons (Eq. (3)). Through the reductive degradation mechanism, these hydrated electrons also degrade the PFOS either by terminal desulfonation (Eq. (6)) or through a nucleophilic attack on the fluorocarbon chain (Tian et al., 2016).

$$Fe - BiOCl + hv \rightarrow h^+ + e^- \text{ or } e^-_{aq} \quad (3)$$

$$O_2 + e^- \rightarrow O_2^{-\bullet} \quad (4)$$

$$O_2^{-\bullet} + O_2^{-\bullet} + 2H^+ \rightarrow H_2O_2 + O_2 \quad (5)$$

$$C_8F_{17}SO_3^- + e^-_{aq} \rightarrow C_8F_{17}^- + SO_3^{-\bullet} \quad (6)$$

$$C_8F_{17}SO_3^- + O_2^{-\bullet} \rightarrow C_8F_{17}^{\bullet} + SO_3^{-\bullet} \quad (7)$$

$$C_8F_{17}^{\bullet} + RRS \rightarrow \text{intermediate products (shorter chains)} \quad (8)$$

Fig. S14 indicates the formation of the intermediates like PFOA, PFHxA, PFHxS, PFHpA, PFHpS, PFPeA, PFPeS, PFBA, and PFBS after 1–3 h of the reaction. This observation is in accord with the commonly reported stepwise degradation pathway. As illustrated in Fig. 6c, the degradation of PFOS is initiated by attacking the terminal –[C–SO_3^-] bond of $C_8F_{17}SO_3H$ by $e^-/O_2^{-\bullet}$ radicals, resulting in the cleavage of the bond and the formation of $^{\bullet}C_8H_{17}$ radical. In accordance with the LCMS data (Fig. S14), the intermediate radical is either oxidized in the presence of molecular oxygen to produce PFOA ($C_7H_{17}COOH$) or undergoes the chain degradation reaction, which results in the formation of shorter-chain PFAS (Eq. (8)). The formation of the shorter-chain PFAS with the sulfonate functionality, such as PFHpS, PFHxS, PFPeS, and PFBS, is possibly due to the reaction of sulfonate radical ($SO_3^{-\bullet}$) (Singh et al., 2019) with corresponding hydrocarbon radicals. According to the time course study and the variation of the concentration of different PFAS, shorter-chain PFAS with sulfonate functionality are formed during the initial stage (1 h) of the degradation reaction, with the possibility of their oxidative conversion to carboxylic counterparts in the later stage. As shown in Fig. 6c, the stepwise desulfonation, decarboxylation, and defluorination continues until the mineralization of PFOS.

4. Conclusions

A carbon modified and Fe-loaded BiOCl ternary composite was prepared through a hydrothermal synthesis route. The carbon modification was confirmed by the Raman spectroscopy and the Fe loading was confirmed by the XPS analysis and elemental mapping of the composite. The introduction of D-Glucose facilitated the control of the growth of the BiOCl particles and the partial reduction of Fe^{3+} to Fe^0 at an elevated hydrothermal temperature. The Fe loading strongly affected the photocatalytic activity of Fe–BiOCl/CS, and the optimal Fe loading was obtained at an Fe:Bi molar ratio of 0.07:4. The optimized Fe–BiOCl/CS was able to effectively photodegrade or defluorinate PFOS both in the direct photocatalytic degradation system and in the two-step adsorption and photodegradation system, resulting in a PFOS degradation of 83.48% and 80.50%, respectively, after 4-h of UV exposure, and a

defluorination of 82.98% and 65.34%. The degradation reaction followed a pseudo-first-order reaction kinetic model. Photogenerated electrons and superoxide radicals were determined as the reactive species responsible for the PFOS degradation. The reaction intermediates revealed a stepwise chain-shortening mechanism involving desulfonation, decarboxylation, and defluorination processes. The new composite material may serve as an effective adsorptive photocatalyst for more cost-effective degradation of PFOS or likely other priority PFAS in water.

CRediT authorship contribution statement

Rayees Ahmad Rather: Conceptualization, Data curation, Methodology, Writing – original draft. **Tianyuan Xu:** Material characterization, Investigation. **Rodney Nelson Leary:** Investigation. **Dongye Zhao:** Supervision, Writing – review & editing, Funding acquisition.

Declaration of competing interest

The authors declare that they have no known competing financial interests or personal relationships that could have appeared to influence the work reported in this paper.

Data availability

Data will be made available on request.

Acknowledgements

This work was partially funded by the National Science Foundation (CBET-2041060) and the Strategic Environmental Research and Development Program (ER18-1515). We are grateful to Dr. Melissa Boersma of Auburn University for analyzing PFOS, Dr. Ingrid Niesman of the SDSU Electron Microscope Facility for the SEM work, and Drs. Lee Blaney and Ke He of University of Maryland Baltimore County for valuable discussion and advice.

Appendix A. Supplementary data

Supplementary data to this article can be found online at https://doi.org/10.1016/j.chemosphere.2023.140585.

References

Aprile, C., Corma, A., Garcia, H., 2008. Enhancement of the photocatalytic activity of TiO_2 through spatial structuring and particle size control: from subnanometric to submillimetric length scale. Phys. Chem. Chem. Phys. 10, 769–783.

Bai, Y., Wang, P.-Q., Liu, J.-Y., Liu, X.-J., 2014. Enhanced photocatalytic performance of direct Z-scheme BiOCl–gC_3N_4 photocatalysts. RSC Adv. 4, 19456–19461.

Boone, J.S., Vigo, C., Boone, T., Byrne, C., Ferrario, J., Benson, R., Donohue, J., Simmons, J.E., Kolpin, D.W., Furlong, E.T., 2019. Per-and polyfluoroalkyl substances in source and treated drinking waters of the United States. Sci. Total Environ. 653, 359–369.

Cao, S., Guo, C., Lv, Y., Guo, Y., Liu, Q., 2009. A novel BiOCl film with flowerlike hierarchical structures and its optical properties. Nanotechnology 20, 275702.

Chen, C., Jiang, T., Hou, J., Zhang, T., Zhang, G., Zhang, Y., Wang, X., 2022. Oxygen vacancies induced narrow band gap of BiOCl for efficient visible-light catalytic performance from double radicals. J. Mater. Sci. Technol. 114, 240–248.

Chen, F., Liu, H., Bagwasi, S., Shen, X., Zhang, J., 2010. Photocatalytic study of BiOCl for degradation of organic pollutants under UV irradiation. J. Photochem. Photobiol., A: Chem 215, 76–80.

Dean, W.S., Adejumo, H.A., Caiati, A., Garay, P.M., Harmata, A.S., Li, L., Rodriguez, E.E., Sundar, S., 2020. A framework for regulation of new and existing PFAS by EPA. J. Sci. Policy Gov. 16, 14.

Dehghani, M., Naseri, M., Nadeem, H., Holl, M.M.B., Batchelor, W., 2022. Sunlight-driven photocatalytic per-and polyfluoroalkyl substances degradation over zinc oxide/cellulose nanofiber catalyst using a continuous flow reactor. J. Environ. Chem. Eng. 10, 108686.

Fang, Y., Meng, P., Schaefer, C., Knappe, D.R., 2023. Removal and destruction of perfluoroalkyl ether carboxylic acids (PFECAs) in an anion exchange resin and electrochemical oxidation treatment train. Water Res. 230, 119522.

Furtado, R.X.d.S., Sabatini, C.A., Zaiat, M., Azevedo, E.B., 2021. Perfluorooctane sulfonic acid (PFOS) degradation by optimized heterogeneous photocatalysis (TiO_2/UV) using the response surface methodology (RSM). J. Water Process Eng. 41, 101986.

Gao, X., Liu, Z., Li, J., Wang, X., Cui, L., Ai, S., Zhao, S., Xu, Q., 2020. Ecological and health risk assessment of perfluorooctane sulfonate in surface and drinking water resources in China. Sci. Total Environ. 738, 139914.

Glüge, J., Scheringer, M., Cousins, I.T., DeWitt, J.C., Goldenman, G., Herzke, D., Lohmann, R., Ng, C.A., Trier, X., Wang, Z., 2020. An overview of the uses of per-and polyfluoroalkyl substances (PFAS). Environ. Sci.: Process. Impacts 22, 2345–2373.

Huang, L., Dong, W., Hou, H., 2007. Investigation of the reactivity of hydrated electron toward perfluorinated carboxylates by laser flash photolysis. Chem. Phy. Lett. 436, 124–128.

Keramidas, K., Voutsas, G., Rentzeperis, P., 1993. The crystal structure of BiOCl. Z. für Kristallogr. - Cryst. Mater. 205, 35–40.

Kucharzyk, K.H., Darlington, R., Benotti, M., Deeb, R., Hawley, E., 2017. Novel treatment technologies for PFAS compounds: a critical review. J. Environ. Manag. 204, 757–764.

Lashuk, B., Pineda, M., AbuBakr, S., Boffito, D., Yargeau, V., 2022. Application of photocatalytic ozonation with a WO_3/TiO_2 catalyst for PFAS removal under UVA/visible light. Sci. Total Environ. 843, 157006.

Leeson, A., Thompson, T., Stroo, H.F., Anderson, R.H., Speicher, J., Mills, M.A., Willey, J., Coyle, C., Ghosh, R., Lebrón, C., 2021. Identifying and managing aqueous film-forming foam-derived per-and polyfluoroalkyl substances in the environment. Environ. Toxicol. Chem. 40, 24–36.

Lei, X., Lian, Q., Zhang, X., Karsili, T.K., Holmes, W., Chen, Y., Zappi, M.E., Gang, D.D., 2023. A review of PFAS adsorption from aqueous solutions: current approaches, engineering applications, challenges, and opportunities. Environ. Pollut., 121138

Lei, Y., Wang, G., Song, S., Fan, W., Zhang, H., 2009. Synthesis, characterization and assembly of BiOCl nanostructure and their photocatalytic properties. CrystEngComm 11, 1857–1862.

Leonello, D., Fendrich, M.A., Parrino, F., Patel, N., Orlandi, M., Miotello, A., 2021. Light-induced advanced oxidation processes as pfas remediation methods: a review. Appl. Sci. 11, 8458.

Li, F., Wei, Z., He, K., Blaney, L., Cheng, X., Xu, T., Liu, W., Zhao, D., 2020. A concentrate-and- destroy technique for degradation of perfluorooctanoic acid in water using a new adsorptive photocatalyst. Water Res. 185, 116219.

Li, H., Qin, F., Yang, Z., Cui, X., Wang, J., Zhang, L., 2017. New reaction pathway induced by plasmon for selective benzyl alcohol oxidation on BiOCl possessing oxygen vacancies. J. Am. Chem. Soc. 139, 3513–3521.

Lin, X., Huang, T., Huang, F., Wang, W., Shi, J., 2006. Photocatalytic activity of a Bi-based oxychloride Bi_3O_4Cl. J. Phys. Chem. B 110, 24629–24634.

Liu, X., Duan, X., Bao, T., Hao, D., Chen, Z., Wei, W., Wang, D., Wang, S., Ni, B.-J., 2022. High- performance photocatalytic decomposition of PFOA by BiOX/TiO_2 heterojunctions: self-induced inner electric fields and band alignment. J. Hazard Mater. 430, 128195.

Liu, X., Xu, B., Duan, X., Hao, Q., Wei, W., Wang, S., Ni, B.-J., 2021. Facile preparation of hydrophilic In_2O_3 nanospheres and rods with improved performances for photocatalytic degradation of PFOA. Environ. Sci.: Nano 8, 1010–1018.

Longendyke, G.K., Katel, S., Wang, Y., 2022. PFAS fate and destruction mechanisms during thermal treatment: a comprehensive review. Environ. Sci.: Process. Impacts 24, 196–208.

McCarthy, C., Kappleman, W., DiGuiseppi, W., 2017. Ecological considerations of per-and polyfluoroalkyl substances (PFAS). Curr. Pollut. Rep. 3, 289–301.

Mi, Y., Wen, L., Wang, Z., Cao, D., Xu, R., Fang, Y., Zhou, Y., Lei, Y., 2016. Fe (III) modified BiOCl ultrathin nanosheet towards high-efficient visible-light photocatalyst. Nano Energy 30, 109–117.

Mirabediny, M., Sun, J., Yu, T.T., Åkermark, B., Das, B., Kumar, N., 2023. Effective PFAS degradation by electrochemical oxidation methods-recent progress and requirement. Chemosphere, 138109.

Morgan, D.J., 2023. Photoelectron spectroscopy of ceria: reduction, quantification and the myth of the vacancy peak in XPS analysis. Surf. Interface Anal. https://doi.org/10.1002/sia.7254 (in press).

Muntwiler, M., Zhu, X., 2008. Image-potential states on the metallic (111) surface of bismuth. New J. Phys. 10, 113018.

Neta, P., Huie, R.E., Ross, A.B., 1988. Rate constants for reactions of inorganic radicals in aqueous solution. J. Phys. Chem. Ref. Data 17, 1027–1284.

Niu, S., Zhang, R., Guo, C., 2020. Oxygen vacancy induced superior visible-light-driven photo- catalytic performance in the BiOCl homojunction. Mater. Chem. Front. 4, 2314–2324.

Panchangam, S.C., Lin, A.Y.-C., Tsai, J.-H., Lin, C.-F., 2009. Sonication-assisted photocatalytic decomposition of perfluorooctanoic acid. Chemosphere 75, 654–660.

Qanbarzadeh, M., Wang, D., Ateia, M., Sahu, S.P., Cates, E.L., 2020. Impacts of reactor configuration, degradation mechanisms, and water matrices on perfluorocarboxylic acid treatment efficiency by the UV/Bi_3O (OH)$(PO_4)_2$ photocatalytic process. ACS ES&T Eng. 1, 239–248.

Rather, R.A., Sarwara, R.K., Das, N., Pal, B., 2019. Impact of reducing and capping agents on carbohydrates for the growth of Ag and Cu nanostructures and their antibacterial activities. Particuology 43, 219–226.

Rather, R.A., Singh, S., Pal, B., 2017. A C3N4 surface passivated highly photoactive Au-TiO_2 tubular nanostructure for the efficient H_2 production from water under sunlight irradiation. Appl. Catal. B Environ. 213, 9–17.

Shearer, C.J., Slattery, A.D., Stapleton, A.J., Shapter, J.G., Gibson, C.T., 2016. Accurate thickness measurement of graphene. Nanotechnology 27, 125704.

Shen, Z., Li, F., Lu, J., Wang, Z., Li, R., Zhang, X., Zhang, C., Wang, Y., Wang, Y., Lv, Z., 2021. Enhanced N_2 photofixation activity of flower-like BiOCl by in situ Fe (III) doped as an activation center. J. Colloid Interface Sci. 584, 174–181.

Singh, R.K., Fernando, S., Baygi, S.F., Multari, N., Thagard, S.M., Holsen, T.M., 2019. Breakdown products from perfluorinated alkyl substances (PFAS) degradation in a plasma-based water treatment process. Environ. Sci. Technol. 53, 2731–2738.

Song, Z., Dong, X., Wang, N., Zhu, L., Luo, Z., Fang, J., Xiong, C., 2017. Efficient photocatalytic defluorination of perfluorooctanoic acid over BiOCl nanosheets via a hole direct oxidation mechanism. Chem. Eng. J. 317, 925–934.
Tariq, M., Li, Y., Li, W., Zhang, Z., Hu, Y., Zhu, M., Jin, H., Li, Y., Skotnicova, K., 2018. Ferromagnetic coupling of Fe^{3+}-VO-Fe^{3+} polarons in Fe-doped ZnO. Ceram. Int. 44, 71–75.
Tian, H., Gao, J., Li, H., Boyd, S.A., Gu, C., 2016. Complete defluorination of perfluorinated compounds by hydrated electrons generated from 3-indole-acetic-acid in organomodified montmorillonite. Sci. Rep. 6, 32949.
Wang, F., Liu, C., Shih, K., 2012. Adsorption behavior of perfluorooctanesulfonate (PFOS) and perfluorooctanoate (PFOA) on boehmite. Chemosphere 89, 1009–1014.
Wang, Q., Lee, S., Choi, H., 2010. Aging study on the structure of Fe^0-nanoparticles: stabilization, characterization, and reactivity. J. Phy. Chem. C 114, 2027–2033.
Wang, X., Liu, X., Liu, G., Zhang, C., Liu, G., Xu, S., Cui, P., Li, D., 2019. Rapid synthesis of BiOCl graded microspheres with highly exposed (110) facets and oxygen vacancies at room temperature to enhance visible light photocatalytic activity. Catal. Comm. 130, 105769.
Wilson, R., 1966. Vacuum thermionic work functions of polycrystalline Be, Ti, Cr, Fe, Ni, Cu, Pt, and type 304 stainless steel. J. Appl. Phy. 37, 2261–2267.
Wood, P.M., 1988. The potential diagram for oxygen at pH 7. Biochem. J. 253, 287.
Wu, Y., Hu, Y., Han, M., Ouyang, Y., Xia, L., Huang, X., Hu, Z., Li, C., 2021. Mechanism insights into the facet-dependent photocatalytic degradation of perfluorooctanoic acid on BiOCl nanosheets. Chem. Eng. J. 425, 130672.
Xiong, J., Cheng, G., Li, G., Qin, F., Chen, R., 2011. Well-crystallized square-like 2D BiOCl nanoplates: mannitol-assisted hydrothermal synthesis and improved visible-light-driven photocatalytic performance. RSC Adv. 1, 1542–1553.
Xu, T., Zhu, Y., Duan, J., Xia, Y., Tong, T., Zhang, L., Zhao, D., 2020. Enhanced photocatalytic degradation of perfluorooctanoic acid using carbon-modified bismuth phosphate composite: effectiveness, material synergy and roles of carbon. Chem. Eng. J. 395, 124991.
Yang, X., Sun, S., Cui, J., Yang, M., Luo, Y., Liang, S., 2021. Synthesis, functional modifications, and diversified applications of hybrid BiOCl-based heterogeneous photocatalysts: a review. Cryst. Growth Des. 21, 6576–6618.
Ye, L., Jin, X., Leng, Y., Su, Y., Xie, H., Liu, C., 2015. Synthesis of black ultrathin BiOCl nanosheets for efficient photocatalytic H2 production under visible light irradiation. J. Power Sources 293, 409–415.
Yin, Y., Yao, Y., Qian, X., Sun, M., Huang, B., He, G., Chen, H., 2022. Fabrication of Fe/BiOCl/RGO with enhanced photocatalytic degradation of ciprofloxacin under visible light irradiation. Mater. Sci. Semicond. 140, 106384.
Yu, H., Xu, L., Wang, P., Wang, X., Yu, J., 2014. Enhanced photoinduced stability and photocatalytic activity of AgBr photocatalyst by surface modification of Fe (III) cocatalyst. Appl. Cata. B: Environ. 144, 75–82.
Yu, L., Wang, L., Xu, W., Chen, L., Fu, M., Wu, J., Ye, D., 2018. Adsorption of VOCs on reduced graphene oxide. J. Environ. Sci. 67, 171–178.
Zhang, G., Chen, M., Li, C., Wu, B., Chen, J., Xiang, W., Wen, X., Zhang, D., Cao, G., Li, W., 2022. Surface spinel and interface oxygen vacancies enhanced lithium-rich layered oxides with excellent electrochemical performances. Chem. Eng. J. 443, 136434.
Zhang, N., Li, L., Shao, Q., Zhu, T., Huang, X., Xiao, X., 2019a. Fe-doped BiOCl nanosheets with light-switchable oxygen vacancies for photocatalytic nitrogen fixation. ACS Appl. Energy Mater. 2, 8394–8398.
Zhang, S., Kang, Q., Peng, H., Ding, M., Zhao, F., Zhou, Y., Dong, Z., Zhang, H., Yang, M., Tao, S., 2019b. Relationship between perfluorooctanoate and perfluorooctane sulfonate blood concentrations in the general population and routine drinking water exposure. Environ. Int. 126, 54–60.
Zhu, Y., Xu, T., Zhao, D., Li, F., Liu, W., Wang, B., An, B., 2021. Adsorption and solid-phase photocatalytic degradation of perfluorooctane sulfonate in water using gallium-doped carbon-modified titanate nanotubes. Chem. Eng. J. 421, 129676.
Zou, Z., Xu, H., Li, D., Sun, J., Xia, D., 2019. Facile preparation and photocatalytic activity of oxygen vacancy rich BiOCl with {0 0 1} exposed reactive facets. Appl. Surf. Sci. 463, 1011–1018.